Report

Neuron

Cortical Circuit Activity Evokes Rapid Astrocyte Calcium Signals on a Similar Timescale to Neurons

Highlights

- A sub-population of astrocyte calcium signals has similar temporal dynamics to neurons
- These fast signals occur in both endfeet and fine processes
- These fast signals are largely independent of IP_3R2 and neuromodulatory pathways

Authors

Jillian L. Stobart, Kim David Ferrari, Matthew J.P. Barrett, Chaim Glück, Michael J. Stobart, Marc Zuend, Bruno Weber

Correspondence

jillian.stobart@umanitoba.ca (J.L.S.), bweber@pharma.uzh.ch (B.W.)

In Brief

Stobart et al. have identified fast astrocyte calcium signals that rapidly follow neuronal signals evoked by whisker stimulation in awake mice. These astrocyte signal dynamics are sufficiently fast to influence cortical information processing and/or neurovascular coupling.

Stobart et al., 2018, Neuron *98*, 726–735
May 16, 2018
https://doi.org/10.1016/j.neuron.2018.03.050

CellPress

CellPress

Neuron
Report

Cortical Circuit Activity Evokes Rapid Astrocyte Calcium Signals on a Similar Timescale to Neurons

Jillian L. Stobart,[1,2,3,*] Kim David Ferrari,[1,2] Matthew J.P. Barrett,[1,2] Chaim Glück,[1,2] Michael J. Stobart,[1,2] Marc Zuend,[1,2] and Bruno Weber[1,2,4,*]

[1]Institute of Pharmacology and Toxicology, University of Zurich, Winterthurerstrasse 190, CH-8057 Zurich, Switzerland
[2]Neuroscience Center, University and ETH Zurich, Winterthurerstrasse 190, CH-8057 Zurich, Switzerland
[3]Present address: College of Pharmacy, University of Manitoba, 750 McDermot Ave., Winnipeg, MB R3E 0T5, Canada
[4]Lead Contact
*Correspondence: jillian.stobart@umanitoba.ca (J.L.S.), bweber@pharma.uzh.ch (B.W.)
https://doi.org/10.1016/j.neuron.2018.03.050

SUMMARY

Sensory stimulation evokes intracellular calcium signals in astrocytes; however, the timing of these signals is disputed. Here, we used novel combinations of genetically encoded calcium indicators for concurrent two-photon imaging of cortical astrocytes and neurons in awake mice during whisker deflection. We identified calcium responses in both astrocyte processes and endfeet that rapidly followed neuronal events (~120 ms after). These fast astrocyte responses were largely independent of IP_3R2-mediated signaling and known neuromodulator activity (acetylcholine, serotonin, and norepinephrine), suggesting that they are evoked by local synaptic activity. The existence of such rapid signals implies that astrocytes are fast enough to play a role in synaptic modulation and neurovascular coupling.

INTRODUCTION

Astrocyte calcium signaling plays a pivotal role in the modulation of synapses (Araque et al., 2014) and local blood flow (Attwell et al., 2010); however, the temporal dynamics of these signals is currently debated (Ding et al., 2013; Gee et al., 2014; Lind et al., 2013, 2018; Nizar et al., 2013; Otsu et al., 2015; Wang et al., 2006; Winship et al., 2007), calling into question the function of astrocytes in these brain processes. Many of these studies have focused on cytosolic calcium signals, primarily in astrocyte somata (Ding et al., 2013; Lind et al., 2013; Nizar et al., 2013; Wang et al., 2006; Winship et al., 2007), but recent work with genetically encoded calcium indicators (GECIs) has identified localized calcium signals within fine astrocyte processes (Agarwal et al., 2017; Bindocci et al., 2017; Lind et al., 2018; Otsu et al., 2015; Srinivasan et al., 2015; Stobart et al., 2018). These microdomains (MDs) can be driven by activation of the circuit and nearby neurons (Bindocci et al., 2017; Stobart et al., 2018) and they may be more relevant for information processing than large-scale calcium events. Fast astrocyte process calcium signals have previously been reported in the CNS of anesthetized mice (Lind et al., 2013, 2018; Otsu et al., 2015), but the evidence for temporal coupling of astrocyte MDs and neurons in awake animals is currently lacking. Furthermore, neuromodulatory pathways (such as the locus coeruleus and nucleus basalis) can evoke large-scale astrocyte calcium responses through mechanisms mediated by G-protein-coupled receptors (GPCRs) and inositol-1,4,5-trisphosphate (IP_3) type 2 receptors (IP_3R2; Chen et al., 2012; Ding et al., 2013; Paukert et al., 2014; Srinivasan et al., 2015; Takata et al., 2011), and this can enhance the responses of astrocytes (Paukert et al., 2014) and neurons to local circuit activity (Chen et al., 2012; Takata et al., 2011). However, the influence of such neurotransmitters on the timing of astrocyte signals is unknown.

Here, we characterized the spatio-temporal calcium dynamics of astrocyte MDs in awake mice and their relationship with nearby neuronal dendrites and somata during different stages of circuit activation (spontaneous or sensory stimulation) to settle the dispute over the timing of astrocyte calcium signals and to better understand the role of these cells in cortical circuits. Our results indicate that fast astrocyte microdomains are evoked by sensory stimulation, and these events are largely independent of neuromodulator activity and IP_3R2-mediated signaling.

RESULTS AND DISCUSSION

We combined GECIs to examine the temporal dynamics of neurons (RCaMP1.07; Ohkura et al., 2012; Pilz et al., 2016) and astrocyte cytosolic MDs (cyto-GCaMP6s; Stobart et al., 2018) or ramified process MDs (Lck-GCaMP6f; Agarwal et al., 2017; Haustein et al., 2014; Institoris et al., 2015) in the layer II/III whisker barrel cortex of awake mice, using two-photon imaging (Figures 1A–1C, details in the STAR Methods). Both GCaMP AAV constructs specifically labeled astrocytes without inducing astrogliosis (Figure S1; Appaix et al., 2012). Regions of interest (ROIs) were selected by hand from visible structures (neuronal somata, astrocyte somata, and astrocyte endfeet) or by an unbiased algorithm that identified active pixels (neuronal dendrites and astrocyte processes; Figures 1D and 1E; Barrett et al., 2018; Ellefsen et al., 2014; Stobart et al., 2018). Single whisker deflection (90 Hz for 8 s, Videos S1 and S2) evoked more ROIs

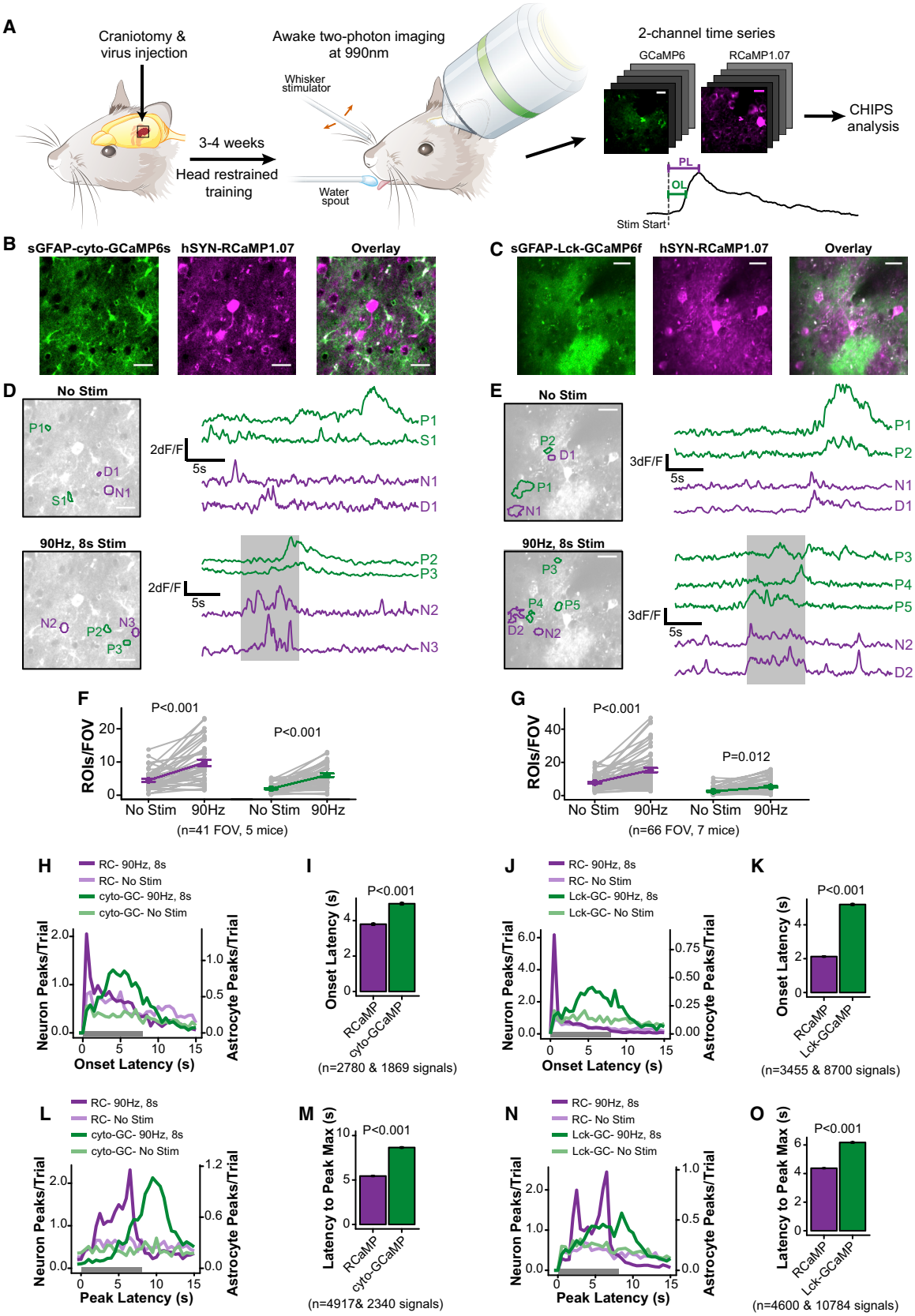

(legend on next page)

in neurons and astrocytes per field of view (Figures 1F and 1G) and increased the mean signal amplitude, signal duration, and the active MD area of both GCaMPs (Figure S2) compared to trials without stimulation. These signaling characteristics were similar to previous reports for these GECIs (Agarwal et al., 2017; Bethge et al., 2017; Srinivasan et al., 2015; Stobart et al., 2018). We also considered the robustness of astrocyte responses over repeated trials by determining the fraction of the total astrocyte area that was active in two or more trials (repeated response [R.R.] score). We observed a high degree of variability in cyto-GCaMP6s repeated responses (Figure S2E), suggesting that the same MDs were not activated during stimulation, similar to our previous results in anesthetized mice (Stobart et al., 2018). However, whisker stimulation increased the repeated response scores from Lck-GCaMP6f expressing cells (Figure S2J), indicating that a larger fraction of the astrocyte area responded to multiple trials of stimulation, possibly due to the proximity of the membrane-tagged GCaMP6f to active synapses.

We next examined the timing of signal peaks relative to the start of whisker stimulation by considering the peak onset latency (defined as the earliest time point at which the fluorescent signal [dF/F] reached 2.5 SD of the baseline) and the latency to peak maximum (the time point of maximal signal amplitude; Figure 1A, lower right) in both neurons and astrocytes. In order to more closely examine the response to stimulation, we only considered signals that occurred before defined time thresholds calculated independently for cyto-GCaMP6s and Lck-GCaMP6f based on the upper bound of the 99% confidence interval of the log-transformed onset or peak latency time distributions (for more details, please see the STAR Methods). Neurons responded to whisker deflection with a peak onset near the start of stimulation (Figures 1H–1K) and reached peak maximum during the stimulus period (Figures 1L–1O). Astrocyte MDs displayed a range of peak onset latencies (Figures 1H and 1J) and latency to peak maximum times (Figures 1L and 1N) that were delayed compared to the neurons (Figures 1I, 1K, 1M, and 1O). These temporal dynamics were similar to previous reports that argue that astrocyte calcium signals are too slow to be involved in mechanisms like neurovascular coupling (Ding et al., 2013; Gee et al., 2014; Nizar et al., 2013; Wang et al., 2006).

Although we detected numerous slow astrocyte calcium signals (Figure 1), we also identified a Lck-GCaMP6f sub-population of fast MDs (8.3% of ROIs; Figures 2A–2C) by considering astrocyte events that occurred within the median onset time of neurons during stimulation (1.098 s). The remaining astrocyte ROIs (with an onset between 1.098 and the Lck-GCaMP6f onset threshold [12.76 s]) were considered delayed MDs. Whisker stimulation evoked more fast MDs (Figure S3C) and these ROIs were not due to bleed-through from the RCaMP channel (Figure S3D). Fast MDs had a peak onset latency on a similar scale to neurons (mean neuronal onset = 270.7 ± 4.3 ms; mean fast MDs onset = 588.5 ± 21.2 ms; mean delayed MDs onset = 5.45 ± 0.05 s; Figure 2E). They also reached maximum amplitude before neurons and delayed MDs (Figure 2F), likely due to the single-event nature of the Lck-GCaMP6f signals, unlike neurons that displayed oscillating calcium signals for the entire duration of the stimulus (traces in Figures 1D and 1E and Figures 2C and 2J). In order to examine the temporal differences between neurons and fast MDs more closely, we identified fast astrocyte ROIs during frame scan image acquisitions and collected line scans over the fast MD areas (Figures 2I and 2J). The mean onset latency of line scan fast astrocyte MDs was not different from neurons (mean neuronal onset = 208.4 ± 26.7 ms; mean fast

Figure 1. Dual-Sensor Two-Photon Calcium Imaging in Neurons and Astrocytes

(A) During surgery, adeno-associated viruses were injected before chronic cranial window implantation. Animals were trained for head-restrained, awake two-photon imaging, using a water reward. Images of GCaMP6 and RCaMP1.07 were collected during 90 Hz single whisker deflection and analyzed using our MATLAB toolbox, Cellular and Hemodynamic Image Processing Suite (CHIPS; Barrett et al., 2018). ROIs were identified by an algorithm for grouping active pixels (astrocyte processes and neuronal dendrites; Ellefsen et al., 2014) or hand-selecting cellular structures (somata [neurons and astrocytes] and endfeet). Signal peaks (lower right) from ROIs were analyzed for amplitude and duration, but also timing relative to stimulus onset (OL, peak onset latency; PL, latency to peak maximum).

(B and C) Example expression of astrocytic cyto-GCaMP6s/neuronal RCaMP1.07 (B) and astrocytic Lck-GCaMP6f/neuronal RCaMP1.07 (C). Scale bars, 20 μm.

(D and E) Example ROIs (left) and traces (right) during no stimulation or whisker stimulation (90 Hz, 8 s) from cells in (B) and (C). Astrocytes (green; p, process; S, soma) and neurons (purple; N, soma; D, dendrite). Traces smoothed by a moving average filter (5-frame: cyto-GCaMP6s/RCaMP1.07; 3-frame: Lck-GCaMP6f/RCaMP1.07). Gray bar indicates stimulation.

(F) Mean number of ROIs/field of view (FOV) during the 8 s stimulus for cyto-GCaMP6s/RCaMP1.07.

(G) Mean number of ROIs/field of view (FOV) during the 8 s stimulus for Lck-GCaMP6f/RCaMP1.07.

(H) Onset latency distributions of cyto-GCaMP6s/RCaMP1.07 (cyto-GC/RC) peaks during no stim and whisker deflection. Stim distributions were different than no stim ($p < 0.001$; Kolmogorov-Smirnov test).

(I) Mean onset latencies for cyto-GC/RC within the cyto-GCaMP6s onset threshold (11.27 s; 5 animals).

(J) Peak onset latency distributions of Lck-GCaMP6f/RCaMP1.07 (Lck-GC/RC) during no stim and whisker deflection. Stim distributions were different than no stim ($p < 0.001$; Kolmogorov-Smirnov test).

(K) Mean onset latency for Lck-GC/RC within the Lck-GCaMP6f onset threshold (12.76 s; 7 animals).

(L) Latency to peak maximum distributions of cyto-GC/RC (no stim and 90 Hz, 8 s). Stim distributions were different than no stim ($p < 0.001$; Kolmogorov-Smirnov test).

(M) Mean latency to peak maximum for cyto-GC/RC within the cyto-GCaMP6s peak max latency threshold (14.74 s; 5 animals).

(N) Latency to peak maximum distributions of Lck-GC/RC (no stim and 90 Hz, 8 s). Stim distributions were different than no stim ($p < 0.001$; Kolmogorov-Smirnov test).

(O) Mean latency to peak maximum for Lck-GC/RC within the Lck-GCaMP6f peak max latency threshold (12.74 s; 7 animals). Horizontal gray bars on all time graphs indicate the stimulus period.

All bar graphs are represented as mean ± SEM and statistics were calculated using linear mixed-effects models and Tukey post hoc tests. See also Figures S1 and S2 and Videos S1 and S2.

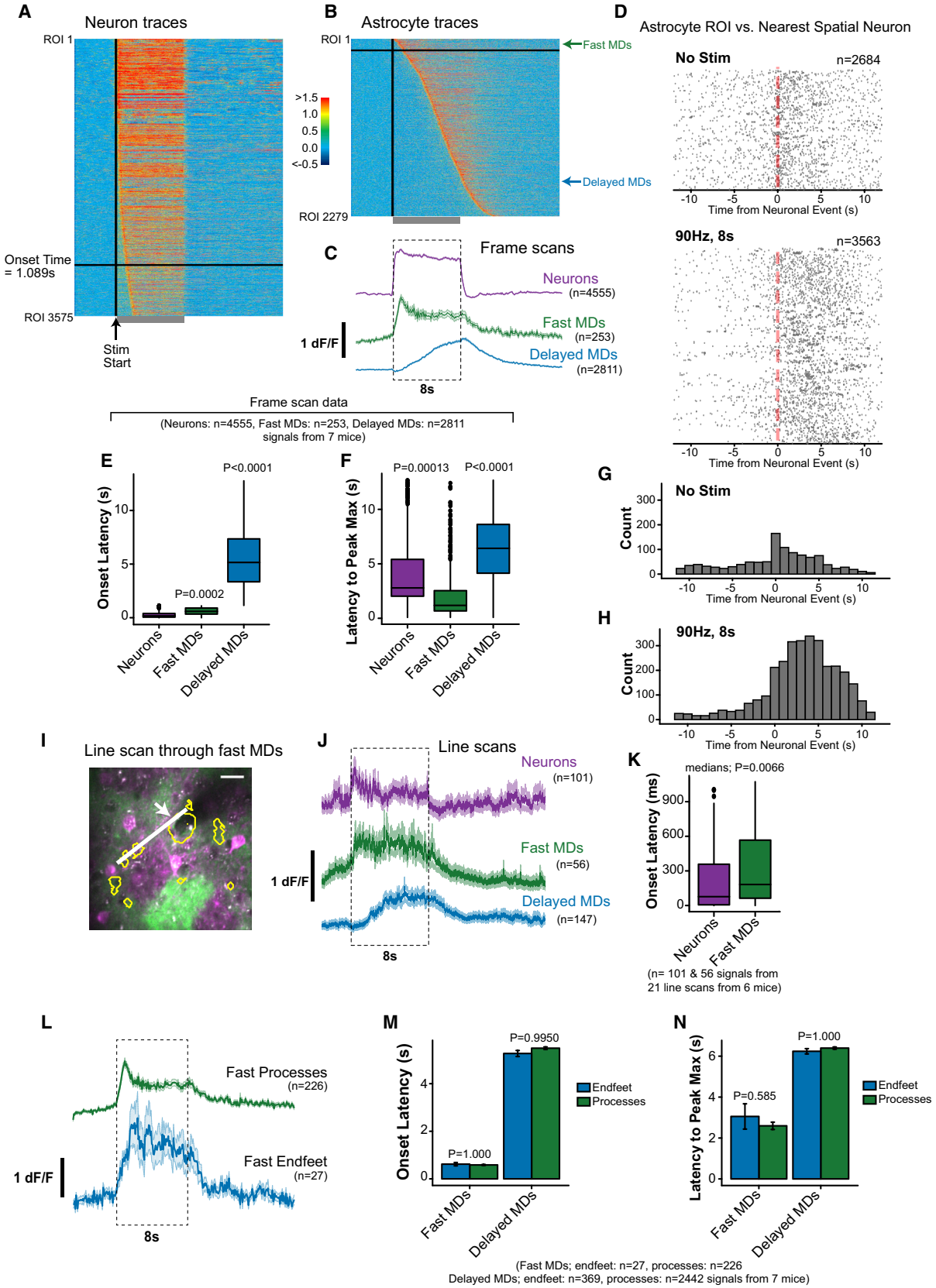

(legend on next page)

MDs onset = 333.1 ± 43 ms, p = 0.205); however, onset times were distributed across the 1.098 s window (Figure 2K) and the median latencies were different (median neuronal onset = 76.6 ms, median fast MD onset = 182.2 ms). GCaMP6f and RCaMP1.07 have comparable rise time kinetics (Chen et al., 2013; Ohkura et al., 2012), suggesting that the difference in peak onset latencies occurred because fast MDs closely followed neurons, and this delay is similar to what has been reported in anesthetized animals (Otsu et al., 2015). Our data suggest that the same fast MDs were activated over repeated trials in the short and long term, particularly because we were able to record fast MD temporal dynamics with line scans over previous fast ROIs. However, statistical analysis of the stability and repeatability of fast MD responses (as in Figure S2) was not possible and requires the acquisition of more stimulation trials in future studies. Fast calcium signals were also detected in endfeet ROIs and they had similar onset latencies and rise times (latency to peak maximum) as fast process MDs (Figures 2L–2N). These characteristics suggest endfeet signals are fast enough to play a role in neurovascular coupling, as has been proposed by other studies (Bindocci et al., 2017; Lind et al., 2013; Otsu et al., 2015).

Fast MDs were also more correlated with active neurons (Figure S3E), which could reflect the close proximity of astrocyte processes and the membrane-tagged GCaMP6f sensor to active synapses (Bindocci et al., 2017). In fact, this fast MD population was only detectable with Lck-GCaMP6f, as the number of fast cyto-GCaMP6s MDs did not increase following stimulation and these ROIs typically had long signals (Figures S3A and S3B). This may explain why other studies, particularly those that used chemical calcium indicators and focused more on large somatic calcium events, have failed to detect rapid astrocyte signals (Ding et al., 2013; Nizar et al., 2013; Wang et al., 2006). It is also possible that we did not detect fast cyto-GCaMP6s signals because we monitored larger fields with numerous neurons and astrocytes, unlike previous work in the olfactory bulb where fast astrocyte transients were detected in fine astrocyte processes with cytosolic GCaMP3 (Otsu et al., 2015).

We also examined astrocyte-neuron temporal coupling during different stages of circuit activity (spontaneous or sensory stimulation) by calculating the peak onset latency difference between each astrocyte ROI and its nearest neighboring neuronal ROI (Figure 2D). During trials without stimulation, astrocyte MDs had a broad distribution of onset time differences relative to neurons, which was centered close to zero (median = 0.338 s; Figure 2G). This suggests that spontaneous astrocyte calcium signals were uncoupled from neuronal activity overall, though a small subset was synchronized with nearby neurons (i.e., a time difference near zero). Upon stimulation, the distribution of astrocyte-neuron onset time differences shifted toward later times (median = 3.463 s) and the number of time differences near zero increased (Figure 2H). This indicates that astrocyte-neuron temporal coupling was altered during local circuit activation, where astrocyte MDs closely followed neighboring neurons, which resulted in an elevated synchrony between the two cell types (time difference near zero). The direct comparison of astrocyte-neuron temporal dynamics was facilitated by the use of two different GECIs to properly segregate sub-cellular compartments in each cell type. This presents an advantage over previous studies using a single calcium indicator, which required data fitting and interpolation to detect fast astrocyte signals (Lind et al., 2013, 2018). We also grouped neuronal ROIs into high, mid, and low responders (Margolis et al., 2012) based on their amplitudes and found that high responders were the most correlated and closely associated with active Lck-GCaMP6f ROIs (Figures S3F and S3G). This indicates that astrocytes may sense the magnitude of neuronal responses, which is potentially an important feature of their role in cortical circuits.

Numerous different ion channels and receptors have been shown to induce astrocyte calcium signals, many through IP_3R2-mediated release from the endoplasmic reticulum (Chen et al., 2012; Ding et al., 2013; Dunn et al., 2013; Malarkey et al., 2008; Rungta et al., 2016; Shigetomi et al., 2011). We repeated our experiments in mice lacking IP_3R2 (Itpr2 or Ip3r2$^{-/-}$ mice) to examine the contribution of these receptors to fast

Figure 2. Sensory Stimulation Evokes Fast and Delayed Astrocyte Calcium Microdomains

(A) Heatmap traces of neuron RCaMP1.07 ROIs with an onset <2 s after the start of stimulation (90 Hz, 8 s; vertical black line), sorted by onset time. ROIs above the horizontal black line have an onset <1.098 s.

(B) Heatmap traces of astrocyte Lck-GCaMPf ROIs with an onset <12 s after the start of stimulation, sorted by onset time. Fast microdomains (MDs) had an onset time <1.098 s (above horizontal black line) and delayed MDs had an onset time between 1.098 and 12.76 s.

(C) Mean traces for neurons, fast MDs, and delayed MDs (SEM traces in light color) collected by frame scan during whisker stimulation (dashed box; 90 Hz, 8 s).

(D) Raster plots of the onset time difference for each astrocyte ROI relative to the nearest neuron in space during trials without stimulation (top) and with whisker stimulation (bottom). The pink dashed line indicates the time of the calcium event of the nearest neuron.

(E and F) Boxplots of onset latencies (E) and latencies to peak maximum (F) for neurons, fast MDs, and delayed MDs from frame scans during trials with stimulation.

(G and H) Histograms of events in (D).

(I) Example field of view where fast ROIs (yellow outlines) were identified. A line scan (white line) was conducted through several fast MDs to get better spatial and temporal resolution of astrocyte/neuron signals. Some line scans also included endfeet (arrow).

(J) Mean traces for neurons, fast MDs, and delayed MDs (SEM traces in light color; data smoothed by 9 frame moving average) collected by line scans during whisker stimulation (dashed box; 90 Hz, 8 s; 21 line scans from 6 mice).

(K) Boxplots of neuron and fast MD onset latencies.

(L) Mean traces for fast processes (green) and endfeet (blue) in response to whisker stimulation (dashed box; 90 Hz, 8 s; SEM indicated by light lines).

(M and N) Mean onset latencies (M) and latencies to peak maximum (N) for fast and delayed endfeet and processes. The timing between endfeet and processes were not significantly different. Boxplots are median and quantile, whiskers: max/min values.

Bar graphs are represented as mean ± SEM. Mean statistics were calculated using linear mixed-effects models and Tukey post hoc tests. Median comparisons were conducted with the Wilcoxon Rank Sum test. See also Figure S3.

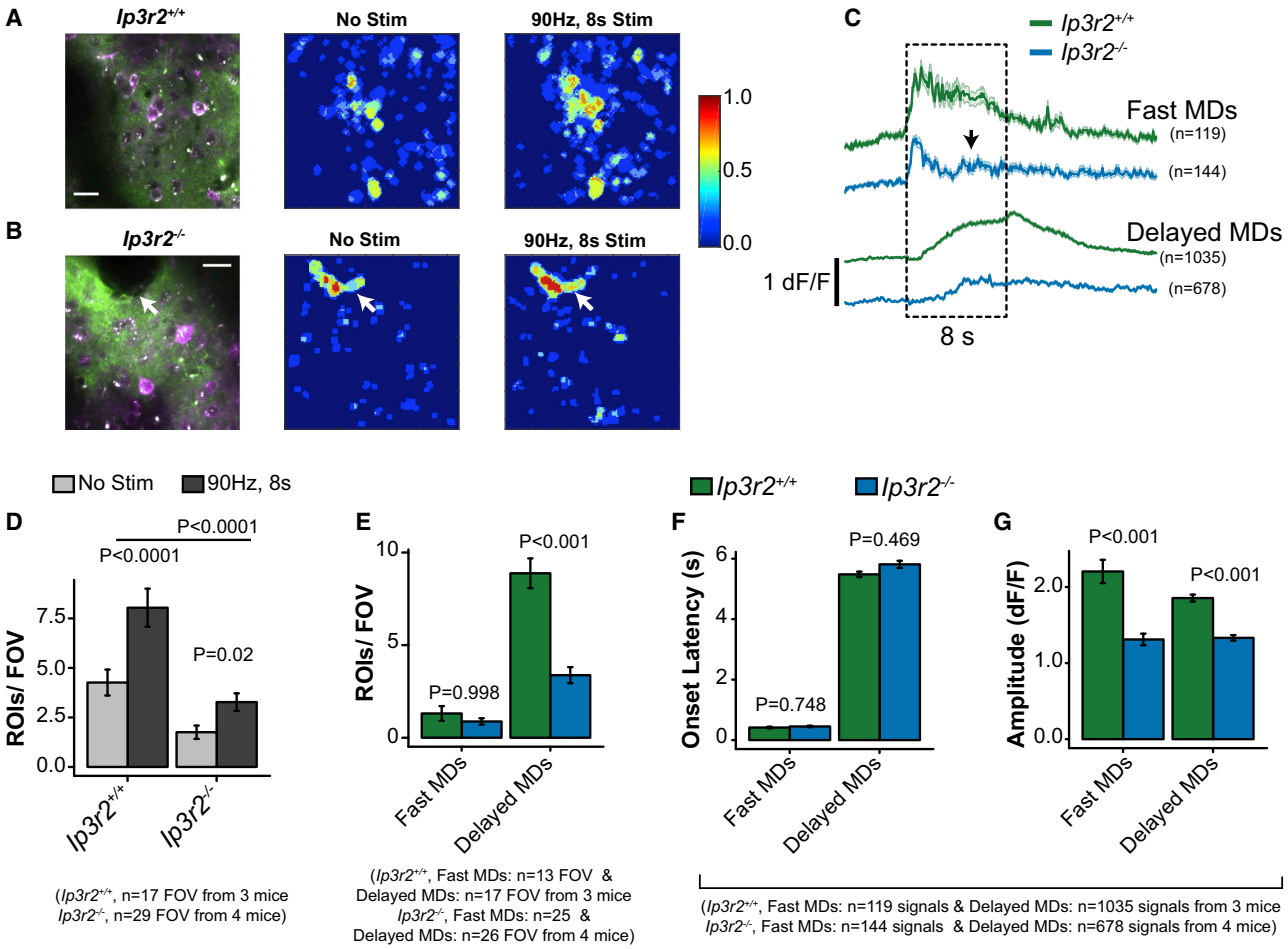

Figure 3. Fast Astrocyte MDs Are Similar between *Ip3r2*$^{-/-}$ Mice and Littermate Controls

(A) Left: example field of view from an *Ip3r2*$^{+/+}$ mouse (littermate control) expressing hSYN-RCaMP1.07 (magenta) and sGFAP-Lck-GCaMP6f (green). Middle and right: response heatmaps generated by overlaying ROI masks from all trials. The scale depicts astrocyte regions that were detected in multiple trials with 1.0 (red) indicating a response in all trials and zero (blue) indicating no ROI detected.

(B) Left: example field of view from an *Ip3r2*$^{-/-}$ mouse (knockout) expressing hSYN-RCaMP1.07 (magenta) and sGFAP-Lck-GCaMP6f (green). Middle and right: response heatmaps generated by overlaying ROI masks from all trials (scale as in A). Notably, repeated responses were detected including in endfeet (arrow).

(C) Mean traces for fast and delayed MDs from *Ip3r2*$^{+/+}$ (green) and *Ip3r2*$^{-/-}$ (blue) littermates in response to whisker stimulation (dashed box; 90 Hz, 8 s; SEM indicated by light lines). The black arrow denotes a decreased amplitude in the knockouts.

(D) Mean number of astrocyte MD ROIs detected in each field of view (FOV) during the 8 s time window of stimulation in *Ip3r2*$^{+/+}$ and *Ip3r2*$^{-/-}$mice.

(E) Mean number of fast and delayed MDs detected in each field of view in *Ip3r2*$^{+/+}$ (green) and *Ip3r2*$^{-/-}$ (blue) mice.

(F and G) Peak onset latencies (F) and mean amplitudes (G) for signals from fast and delayed MDs in *Ip3r2*$^{+/+}$ (green) and *Ip3r2*$^{-/-}$ (blue) mice. These data are from frame scans, as line scan results were similar (data not shown).

Bar graphs are represented as mean ± SEM. Mean statistics were calculated using linear mixed-effects models and Tukey post hoc tests.

astrocyte MDs. These mice had fewer astrocyte MDs compared to littermate controls (Agarwal et al., 2017; Srinivasan et al., 2015; Stobart et al., 2018), but whisker stimulation evoked an increased number of active MDs (Figures 3A, 3B, and 3D; Stobart et al., 2018). We detected fewer delayed MDs (defined as in Figure 2) in Ip3r2$^{-/-}$ mice, though their mean onset latency was not different from delayed MDs in controls (Ip3r2$^{+/+}$; Figures 3E and 3F). This suggests that IP_3-mediated signaling significantly contributes to the prevalence of these delayed events. The remaining ~21% of the MD population were fast and the number of these MDs per field of view and their mean onset latency were not different between Ip3r2$^{-/-}$ and controls (Ip3r2$^{+/+}$; Figures 3E and 3F). Nevertheless, we observed a reduction in signal amplitude in both fast and delayed MDs (see arrow in Figures 3C and 3G), suggesting that a component of fast MDs involves IP_3R2-mediated signaling, but that this does not affect the rapid temporal dynamics. While these knockout mice have been used extensively in the field to study astrocyte calcium, it is important to note that they have normal synaptic plasticity (Agulhon et al., 2010) and behavior phenotypes (Petravicz et al., 2014) and we also did not detect a change in neuronal responses to stimulation (data not shown). Furthermore, recent evidence indicates that GPCR-mediated calcium signaling is preserved in Ip3r2$^{-/-}$ mice (Srinivasan et al., 2015) and that

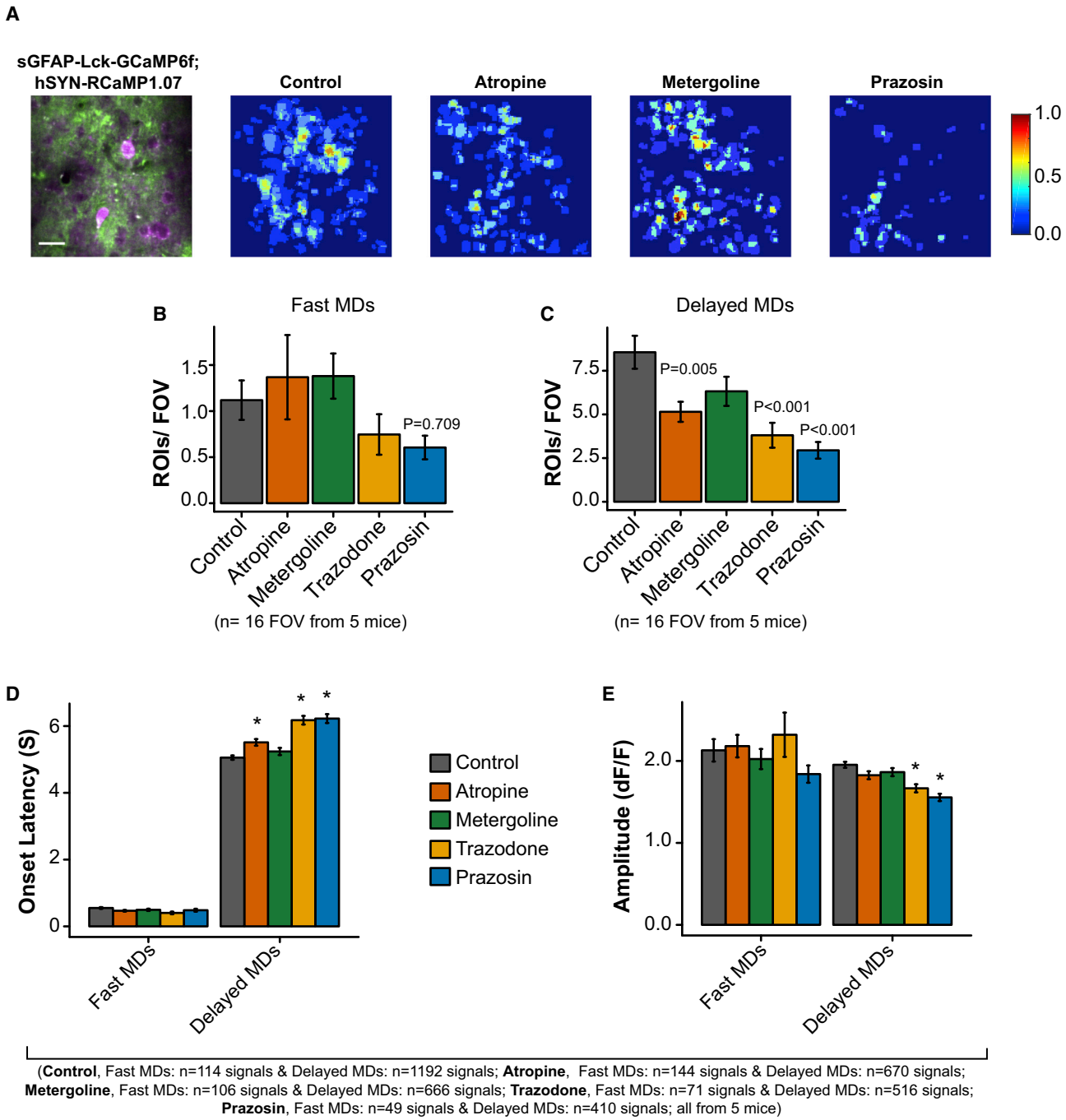

Figure 4. Fast Astrocyte MDs Are Not Significantly Altered by Neuromodulator Receptor Blockade

(A) Left: example field of view expressing hSYN-RCaMP1.07 (magenta) and sGFAP-Lck-GCaMP6f (green). Right: response heatmaps from the same field of view during different pharmacological treatments: control (no injection) and atropine, metergoline, and prazosin. The scale depicts astrocyte regions that were detected in multiple trials with 1.0 (red) indicating a response in all trials and zero (blue) indicating no ROI detected.

(B) Mean number of fast MDs evoked in each field of view by whisker stimulation following pharmacological treatment (atropine: 5 mg/kg, metergoline: 5 mg/kg, trazodone: 10 mg/kg, and prazosin: 1 mg/kg; all administered i.p. at least 20 min before imaging).

(C) Mean number of delayed MDs detected in each field of view during stimulation trials and following drug injection.

(D and E) Peak onset latencies and mean amplitudes for signals from fast and delayed MDs during pharmacological treatment. These data are from frame scans; line scan results were similar (data not shown). *$p < 0.01$.

Bar graphs are represented as mean ± SEM. Mean statistics were calculated using linear mixed-effects models and Tukey post hoc tests. All pharmacological comparisons were relative to control bars. See also Figure S4.

other IP_3 receptors (IP_3R1 and IP_3R3) underlie localized transients in astrocyte processes (Sherwood et al., 2017). Thus, we cannot rule out a role for GPCRs and IP_3-mediated signaling in fast astrocyte MDs.

Neuromodulatory pathways, such as norepinephrine projections from the locus coeruleus and cholinergic innervation from the basal forebrain, can induce large-scale astrocyte calcium transients (Chen et al., 2012; Ding et al., 2013; Paukert et al., 2014; Srinivasan et al., 2015; Takata et al., 2011) and influence neuronal responses to local circuit activation (Sara, 2009). We assessed whether neuromodulatory antagonists attenuated fast and delayed astrocyte MDs evoked by whisker stimulation, by imaging the same cell populations before and after intraperitoneal (i.p.) injection of specific blockers (Figure 4 and Figure S4). Drugs that affect norepinephrine signaling (trazodone, a broad-spectrum inhibitor of adrenergic, serotonergic, and histaminergic receptors, prazosin, a selective α_1-adrenergic receptor blocker, and DSP4, a locus coeruleus neurotoxin) reduced the total number of astrocyte signals that we detected (Figure 4A and Figure S4A), by inhibiting delayed MDs but not fast MDs (Figures 4B and 4C and Figures S4B and S4C). These drugs also increased the onset latency and decreased the amplitude of delayed MDs, without affecting the timing and amplitude of fast MDs (Figures 4E and 4F and Figures S4D and S4E). This suggests that norepinephrine can influence astrocyte responses to cortical circuits, particularly on longer timescales, but that fast MDs are mediated by local synaptic activity and not strictly by "startle" of the animal (Ding et al., 2013; Paukert et al., 2014; Srinivasan et al., 2015). Atropine, a muscarinic receptor antagonist, had effects similar to norepinephrine antagonists and also reduced the number of delayed MDs and increased their onset latency, without affecting fast MDs (Figure 4). This indicates that basal forebrain cholinergic pathways can also influence astrocytes on longer timescales, without changing rapid responses to local barrel circuits, which has important implications for the role of astrocytes in attention and cognitive processing. Finally, we did not observe effects of metergoline, a serotonin receptor antagonist, on astrocyte calcium signals evoked by whisker stimulation, though we did detect an overall increase in astrocyte spontaneous activity (Figure S4C), possibly due to the dopamine receptor agonist activity of this drug. Also, in most cases, these neuromodulatory drugs did not significantly change neuronal responses, though DSP4 decreased spontaneous neuronal activity (Figure S4F) and trazodone and metergoline reduced the number of neuronal signals evoked by whisker stimulation (Figure S4G). Our results provide the necessary first steps to clearly show that fast astrocyte responses are evoked by cortical circuit activity, without significant influence of neuromodulatory pathways, and detailed studies of the underlying signaling of these fast signals will follow in future studies.

In summary and to the best of our knowledge, we have identified, for the first time, fast astrocyte calcium microdomains in fine processes and endfeet that closely follow nearby neuronal activity evoked by sensory stimulation in awake mice. These observations were made possible by the increased sensitivity of membrane-anchored GCaMP6f to microdomain signals, which likely explains why previous studies reported only delayed signals (Ding et al., 2013; Gee et al., 2014; Nizar et al., 2013; Stobart et al., 2018; Wang et al., 2006). In addition, combining astrocytic GCaMP6f with neuronal RCaMP1.07 allowed us to distinguish each cell population uniquely and to more closely examine different sub-cellular compartments, which are significant improvements over previous studies (Lind et al., 2013, 2018). This work provides new insight into the timing of activity in astrocyte and neuron fine structures and suggests that astrocyte activity is fast enough to play a key role in fundamental brain functions, such as synaptic modulation or neurovascular coupling.

STAR★METHODS

Detailed methods are provided in the online version of this paper and include the following:

- KEY RESOURCES TABLE
- CONTACT FOR REAGENT AND RESOURCE SHARING
- EXPERIMENTAL MODEL AND SUBJECT DETAILS
  - Animals
- METHOD DETAILS
  - Cloning and virus production
  - Surgery and virus injection
  - Intrinsic optical imaging
  - Behavior training
  - Awake two-photon imaging
  - *In vivo* pharmacology
  - SR101 staining
  - Immunohistochemistry
- QUANTIFICATION AND STATISTICAL ANALYSIS
- DATA AND SOFTWARE AVAILABILITY

SUPPLEMENTAL INFORMATION

Supplemental Information includes four figures and two videos and can be found with this article online at https://doi.org/10.1016/j.neuron.2018.03.050.

A video abstract is available at https://doi.org/10.1016/j.neuron.2018.03.050#mmc5.

ACKNOWLEDGMENTS

We would like to thank Aiman Saab and Zoe Looser for mouse breeding and genotyping support. We would also like to thank Jean-Marc Fritschy and his laboratory for help with immunohistochemistry and Steven Brown and his group for molecular biology support. B.W. is supported by the Swiss National Science Foundation (SNF Number: 31003A_156965) and is a member of the Clinical Research Priority Program of the University of Zurich on Molecular Imaging.

AUTHOR CONTRIBUTIONS

Conceptualization, J.L.S. and B.W.; Methodology, M.Z..; Software, M.J.P.B., K.D.F., and J.L.S.; Investigation, J.L.S., K.D.F., C.G., and M.J.S.; Formal Analysis, J.L.S., K.D.F., and M.J.P.B.; Writing – Original Draft J.L.S.; Writing – Review & Editing, J.L.S., M.J.P.B., K.D.F., and B.W.; Funding Acquisition, B.W.

DECLARATION OF INTERESTS

The authors declare no competing interests.

Received: September 25, 2017
Revised: February 12, 2018
Accepted: March 30, 2018
Published: April 26, 2018

REFERENCES

Agarwal, A., Wu, P.-H., Hughes, E.G., Fukaya, M., Tischfield, M.A., Langseth, A.J., Wirtz, D., and Bergles, D.E. (2017). Transient opening of the mitochondrial permeability transition pore induces microdomain calcium transients in astrocyte processes. Neuron *93*, 587–605.e7.

Agulhon, C., Fiacco, T.A., and McCarthy, K.D. (2010). Hippocampal short- and long-term plasticity are not modulated by astrocyte Ca2+ signaling. Science *327*, 1250–1254.

Appaix, F., Girod, S., Boisseau, S., Römer, J., Vial, J.C., Albrieux, M., Maurin, M., Depaulis, A., Guillemain, I., and van der Sanden, B. (2012). Specific in vivo staining of astrocytes in the whole brain after intravenous injection of sulforhodamine dyes. PLoS ONE *7*, e35169.

Araque, A., Carmignoto, G., Haydon, P.G., Oliet, S.H.R., Robitaille, R., and Volterra, A. (2014). Gliotransmitters travel in time and space. Neuron *81*, 728–739.

Attwell, D., Buchan, A.M., Charpak, S., Lauritzen, M., Macvicar, B.A., and Newman, E.A. (2010). Glial and neuronal control of brain blood flow. Nature *468*, 232–243.

Barrett, M.J.P., Ferrari, K.D., Stobart, J.L., Holub, M., and Weber, B. (2018). CHIPS: an extensible toolbox for cellular and hemodynamic two-photon image analysis. Neuroinformatics *16*, 145–147.

Bethge, P., Carta, S., Lorenzo, D.A., Egolf, L., Goniotaki, D., Madisen, L., Voigt, F.F., Chen, J.L., Schneider, B., Ohkura, M., et al. (2017). An R-CaMP1.07 reporter mouse for cell-type-specific expression of a sensitive red fluorescent calcium indicator. PLoS ONE *12*, e0179460.

Bindocci, E., Savtchouk, I., Liaudet, N., Becker, D., Carriero, G., and Volterra, A. (2017). Three-dimensional Ca^{2+}imaging advances understanding of astrocyte biology. Science *356*, eaai8185.

Chen, N., Sugihara, H., Sharma, J., Perea, G., Petravicz, J., Le, C., and Sur, M. (2012). Nucleus basalis-enabled stimulus-specific plasticity in the visual cortex is mediated by astrocytes. Proc. Natl. Acad. Sci. USA *109*, E2832–E2841.

Chen, T.-W., Wardill, T.J., Sun, Y., Pulver, S.R., Renninger, S.L., Baohan, A., Schreiter, E.R., Kerr, R.A., Orger, M.B., Jayaraman, V., et al. (2013). Ultrasensitive fluorescent proteins for imaging neuronal activity. Nature *499*, 295–300.

Ding, F., O'Donnell, J., Thrane, A.S., Zeppenfeld, D., Kang, H., Xie, L., Wang, F., and Nedergaard, M. (2013). α1-Adrenergic receptors mediate coordinated Ca^{2+} signaling of cortical astrocytes in awake, behaving mice. Cell Calcium *54*, 387–394.

Dunn, K.M., Hill-Eubanks, D.C., Liedtke, W.B., and Nelson, M.T. (2013). TRPV4 channels stimulate Ca^{2+}-induced Ca^{2+} release in astrocytic endfeet and amplify neurovascular coupling responses. Proc. Natl. Acad. Sci. USA *110*, 6157–6162.

Ellefsen, K.L., Settle, B., Parker, I., and Smith, I.F. (2014). An algorithm for automated detection, localization and measurement of local calcium signals from camera-based imaging. Cell Calcium *56*, 147–156.

Gee, J.M., Smith, N.A., Fernandez, F.R., Economo, M.N., Brunert, D., Rothermel, M., Morris, S.C., Talbot, A., Palumbos, S., Ichida, J.M., et al. (2014). Imaging activity in neurons and glia with a *Polr2a*-based and cre-dependent GCaMP5G-IRES-tdTomato reporter mouse. Neuron *83*, 1058–1072.

Haustein, M.D., Kracun, S., Lu, X.H., Shih, T., Jackson-Weaver, O., Tong, X., Xu, J., Yang, X.W., O'Dell, T.J., Marvin, J.S., et al. (2014). Conditions and constraints for astrocyte calcium signaling in the hippocampal mossy fiber pathway. Neuron *82*, 413–429.

Institoris, Á., Rosenegger, D.G., and Gordon, G.R. (2015). Arteriole dilation to synaptic activation that is sub-threshold to astrocyte endfoot Ca^{2+} transients. J. Cereb. Blood Flow Metab. *35*, 1411–1415.

Li, X., Zima, A.V., Sheikh, F., Blatter, L.A., and Chen, J. (2005). Endothelin-1-induced arrhythmogenic Ca2+ signaling is abolished in atrial myocytes of inositol-1,4,5-trisphosphate(IP3)-receptor type 2-deficient mice. Circ. Res. *96*, 1274–1281.

Lind, B.L., Brazhe, A.R., Jessen, S.B., Tan, F.C.C., and Lauritzen, M.J. (2013). Rapid stimulus-evoked astrocyte Ca^{2+} elevations and hemodynamic responses in mouse somatosensory cortex *in vivo*. Proc. Natl. Acad. Sci. USA *110*, E4678–E4687.

Lind, B.L., Jessen, S.B., Lønstrup, M., Joséphine, C., Bonvento, G., and Lauritzen, M. (2018). Fast Ca^{2+}responses in astrocyte end-feet and neurovascular coupling in mice. Glia *66*, 348–358.

Mächler, P., Wyss, M.T., Elsayed, M., Stobart, J., Gutierrez, R., von Faber-Castell, A., Kaelin, V., Zuend, M., San Martín, A., Romero-Gómez, I., et al. (2016). In vivo evidence for a lactate gradient from astrocytes to neurons. Cell Metab. *23*, 94–102.

Malarkey, E.B., Ni, Y., and Parpura, V. (2008). Ca2+ entry through TRPC1 channels contributes to intracellular Ca2+ dynamics and consequent glutamate release from rat astrocytes. Glia *56*, 821–835.

Margolis, D.J., Lütcke, H., Schulz, K., Haiss, F., Weber, B., Kügler, S., Hasan, M.T., and Helmchen, F. (2012). Reorganization of cortical population activity imaged throughout long-term sensory deprivation. Nat. Neurosci. *15*, 1539–1546.

Mayrhofer, J.M., Haiss, F., Haenni, D., Weber, S., Zuend, M., Barrett, M.J.P., Ferrari, K.D., Maechler, P., Saab, A.S., Stobart, J.L., et al. (2015). Design and performance of an ultra-flexible two-photon microscope for in vivo research. Biomed. Opt. Express *6*, 4228–4237.

Nizar, K., Uhlirova, H., Tian, P., Saisan, P.A., Cheng, Q., Reznichenko, L., Weldy, K.L., Steed, T.C., Sridhar, V.B., MacDonald, C.L., et al. (2013). *In vivo* stimulus-induced vasodilation occurs without IP_3 receptor activation and may precede astrocytic calcium increase. J. Neurosci. *33*, 8411–8422.

Ohkura, M., Sasaki, T., Kobayashi, C., Ikegaya, Y., and Nakai, J. (2012). An improved genetically encoded red fluorescent Ca^{2+} indicator for detecting optically evoked action potentials. PLoS ONE *7*, e39933.

Otsu, Y., Couchman, K., Lyons, D.G., Collot, M., Agarwal, A., Mallet, J.M., Pfrieger, F.W., Bergles, D.E., and Charpak, S. (2015). Calcium dynamics in astrocyte processes during neurovascular coupling. Nat. Neurosci. *18*, 210–218.

Paukert, M., Agarwal, A., Cha, J., Doze, V.A., Kang, J.U., and Bergles, D.E. (2014). Norepinephrine controls astroglial responsiveness to local circuit activity. Neuron *82*, 1263–1270.

Petravicz, J., Boyt, K.M., and McCarthy, K.D. (2014). Astrocyte IP3R2-dependent Ca(2+) signaling is not a major modulator of neuronal pathways governing behavior. Front. Behav. Neurosci. *8*, 384.

Pilz, G.-A., Carta, S., Stäuble, A., Ayaz, A., Jessberger, S., and Helmchen, F. (2016). Functional imaging of dentate granule cells in the adult mouse hippocampus. J. Neurosci. *36*, 7407–7414.

Rungta, R.L., Bernier, L.P., Dissing-Olesen, L., Groten, C.J., LeDue, J.M., Ko, R., Drissler, S., and MacVicar, B.A. (2016). Ca^{2+}transients in astrocyte fine processes occur via Ca^{2+}influx in the adult mouse hippocampus. Glia *64*, 2093–2103.

Sara, S.J. (2009). The locus coeruleus and noradrenergic modulation of cognition. Nat. Rev. Neurosci. *10*, 211–223.

Sherwood, M.W., Arizono, M., Hisatsune, C., Bannai, H., Ebisui, E., Sherwood, J.L., Panatier, A., Oliet, S.H.R., and Mikoshiba, K. (2017). Astrocytic IP_3Rs: Contribution to Ca^{2+}signalling and hippocampal LTP. Glia *65*, 502–513.

Shigetomi, E., Tong, X., Kwan, K.Y., Corey, D.P., and Khakh, B.S. (2011). TRPA1 channels regulate astrocyte resting calcium and inhibitory synapse efficacy through GAT-3. Nat. Neurosci. *15*, 70–80.

Srinivasan, R., Huang, B.S., Venugopal, S., Johnston, A.D., Chai, H., Zeng, H., Golshani, P., and Khakh, B.S. (2015). $Ca(^{2+})$ signaling in astrocytes from $Ip3r2^{(-/-)}$ mice in brain slices and during startle responses in vivo. Nat. Neurosci. *18*, 708–717.

Stobart, J.L., Ferrari, K.D., Barrett, M.J.P., Stobart, M.J., Looser, Z.J., Saab, A.S., and Weber, B. (2018). Long-term in vivo calcium imaging of astrocytes reveals distinct cellular compartment responses to sensory stimulation. Cereb. Cortex *28*, 184–198.

Takata, N., Mishima, T., Hisatsune, C., Nagai, T., Ebisui, E., Mikoshiba, K., and Hirase, H. (2011). Astrocyte calcium signaling transforms cholinergic modulation to cortical plasticity in vivo. J. Neurosci. *31*, 18155–18165.

Wang, X., Lou, N., Xu, Q., Tian, G.-F., Peng, W.G., Han, X., Kang, J., Takano, T., and Nedergaard, M. (2006). Astrocytic Ca^{2+} signaling evoked by sensory stimulation *in vivo*. Nat. Neurosci. *9*, 816–823.

Winship, I.R., Plaa, N., and Murphy, T.H. (2007). Rapid astrocyte calcium signals correlate with neuronal activity and onset of the hemodynamic response *in vivo*. J. Neurosci. *27*, 6268–6272.

STAR★METHODS

KEY RESOURCES TABLE

REAGENT or RESOURCE	SOURCE	IDENTIFIER
Antibodies		
Rabbit anti-GFAP	Dako Cytomation	Dako Cat# Z0334, RRID: AB_10013382
Chicken anti-GFP	Aves Labs	Aves Labs Cat# GFP-1020, RRID: AB_10000240
Goat anti-rabbit Cy5	Jackson ImmunoResearch	Jackson ImmunoResearch Labs Cat# 111-175-003, RRID: AB_2314269
Goat anti-chicken Alexa Fluor 488 Cy5	Thermofisher Scientific	Molecular Probes Cat# A-11039, RRID: AB_142924
Bacterial and Virus Strains		
AAV2/9-hSYN-RCaMP1.07	Custom preparation by the University of North Carolina Vector Core (now available at the University of Zurich Viral Vector Facility)	v224
AAV2/9-gfaABC1D-GCaMP6s	Stobart et al., 2018 (now available at the University of Zurich Viral Vector Faciility	v207
AAV2/5-gfaABC1D-Lck-GCaMP6f	University of Pennsylvania Viral Vector Core	Lot V4378MI-R
Chemicals, Peptides, and Recombinant Proteins		
Sulforhodamine 101	ThermoFisher	Cat. No. S359
Atropine	Sigma-Aldrich	A0132-1G
Metergoline	Sigma-Aldrich	M3668-500MG
N-(2-chloroethyl)-N-ethyl-2-bromobenzylamine, DSP-4	Tocris Bioscience	Cat. No. 2958
Prazosin hydrochloride	Tocris Bioscience	Cat. No. 0623
Trazodone hydrochloride	Sigma-Aldrich	T6154-1G
Experimental Models: Organisms/Strains		
C57BL/6J mice	Charles River	N/A
Itpr2tm1Chen/Itpr2+ (Ip3r2 knockout mice)	Dr. Ju Chen	RRID: MGI:3713675
Recombinant DNA		
pGP-CMV-GCaMP6s	Chen et al., 2013	Addgene 40753
pEF1a-RCaMP1.07	Ohkura et al., 2012	N/A
pAAV-hSYN-RCaMP1.07	This paper (now available at the University of Zurich Viral Vector Facility)	v224
pAAV- gfaABC1D –GCaMP6s	This paper (now available at the University of Zurich Viral Vector Facility)	v207
Software and Algorithms		
MATLAB (R2014b)	MathWorks	RRID: SCR_001622
Cellular and Hemodynamic Image Processing Suite	Barrett et al., 2018	https://ein-lab.github.io/
ImageJ	https://imagej.nih.gov/ij/	RRID: SCR_003070
R (version 3.2.5)	https://www.r-project.org/	N/A
RStudio (version 1.0.136)	https://www.rstudio.com/products/rstudio/download/	N/A

CONTACT FOR REAGENT AND RESOURCE SHARING

Requests for further information, reagents, and resources should be directed to Dr. Bruno Weber (bweber@pharma.uzh.ch). All published reagents will be shared in full.

EXPERIMENTAL MODEL AND SUBJECT DETAILS

Animals

Female C57BL/6J (Charles River) or Ip3r2$^{-/-}$ and litter mate controls; Ip3r2$^{+/+}$ (Itpr2^{tm1Chen} ; Li et al., 2005) were housed under an inverted 12-hr light/dark cycle. Genotyping of Ip3r2 mice was conducted as described previously (Li et al., 2005; Stobart et al., 2018). Each animal underwent surgery at 8-10 weeks old, training for the head-restraint/water reward paradigm, and imaging regularly (3-4 times per week) under the two-photon microscope for up to 5 months. Procedures were approved by the local veterinary authorities, conforming to the guidelines of the Swiss Animal Protection Law, Veterinary Office, Canton Zurich (Act of Animal Protection 16 December 2005 and Animal Protection Ordinance 23 April 2008).

METHOD DETAILS

Cloning and virus production

The RCaMP1.07 gene (Ohkura et al., 2012; Pilz et al., 2016) was cloned into a plasmid backbone containing adeno-associated virus (AAV2) inverted terminal repeats and the human synapsin (hSYN) promoter (Mächler et al., 2016). The GCaMP6s gene (Addgene plasmid #40753; Chen et al., 2013) was cloned into a plasmid backbone containing a shorted glial fibrillary acidic protein (gfaABC1D) promoter (Mächler et al., 2016; Stobart et al., 2018). These plasmids were packaged into AAV serotype 9 (AAV2/9-hSYN-RCaMP1.07 and AAV2/9- gfaABC1D-GCaMP6s by the University of North Carolina Vector Core. AAV2/5-gfaABC1D-Lck-GCaMP6f was purchased from the University of Pennsylvania Viral Vector Core.

Surgery and virus injection

The surgery was conducted as previously described (Stobart et al., 2018). On the first day, animals were fitted with a dental cement head cap (Tetric EvoFlow; polymerized with blue light) and custom-made aluminum head post, while under isoflurane (4% for induction, 1%–2% for maintenance). On the second day, the animal was anesthetized with midazolam (5 mg/kg), fentanyl (0.05 mg/kg) and medetomidine (0.5 mg/kg), and a craniotomy was cut over the barrel cortex using the intrinsic optical imaging map as a reference (see details below). A pipette and hydraulic pump were used to inject virus (300 nL at 50 nL/min) at a depth of 400 – 500 μm into two different whisker areas. The approximate virus concentration in each mix was: a) 2.4×10^{12} particles/ml of AAV2/9-hSYN-RCaMP1.07 and 1.6×10^{12} particles/mL of AAV2/9-gfaABC1D-GCaMP6s and b) 2.4×10^{12} particles/mL of AAV2/9-hSYN-RCaMP1.07 and 1.2×10^{12} particles/mL of AAV2/5-gfaABC1D-Lck-GCaMP6f. A square coverslip (3x3 mm) was lightly pressed on the exposed brain and fixed with dental cement to the head cap. The animal was given buprenorphine (0.1 mg/kg) for 3 days following the surgery.

Intrinsic optical imaging

The whisker barrel area in the left somatosensory cortex was mapped by intrinsic optical imaging (IOI; see details below) through the skull (before craniotomy) or the cranial window (before two-photon imaging) to identify specific whisker areas. Under 630 nm illumination, images were acquired using a 12-bit CCD camera (Pixelfly VGA, PCO Imaging) focused 400 μm below the cortical surface. The brain region activated by a single whisker deflection (10 Hz, 6 s) was identified by increased light absorption (due to increased blood flow).

Behavior training

One week after surgery, training for awake two-photon imaging commenced. First, the animals were handled several times a day for 3-5 days until they were comfortable with the experimenter. Then, they were introduced to the head fixation box by restraining them via the implanted head post multiple times a day starting with restraint for several seconds up to several minutes. Following multiple days of such acclimatization, the animals were deprived of water overnight and presented with water from a lick spout while head restrained. Once the animals licked freely from the spout, a water drop was presented in sync with an auditory cue at the end of a 10 s trial. The goal was to train the animal to sit still and become accustomed to a whisker stimulus during the trial, whereby they received water as a reward. The whisker stimulus was presented by threading a single whisker into a glass capillary affixed to a piezo element (T223-H4CL-303X; Piezo Systems) vibrated at 90 Hz. Once the animal learned to sit still for the duration of the trial, the length of trials was increased to 90 s. The total time to train each animal was 3-4 weeks.

Awake two-photon imaging

Animals were imaged while performing the water reward task under a custom-built two-photon laser-scanning microscope (Mayrhofer et al., 2015) with a 20x water immersion objective (W Plan-Apochromat 20x/1.0 DIC VIS-IR, Zeiss). RCaMP1.07 and

GCaMP6 were excited at 990 nm with a Ti:sapphire laser (Mai Tai; Spectra-Physics), and emission was detected with GaAsP photomultiplier modules (Hamamatsu Photonics) fitted with 520/50 nm band pass filter or a 607/70 band pass filter and separated by a 560 nm dichroic mirror (BrightLine; Semrock). The microscope was controlled by a customised version of *ScanImage* (r3.8.1; Janelia Research Campus).

At the beginning of each imaging session, short trials (10 s) with 1 s of whisker stimulation (90Hz) were used to identify one or two fields of view in cortical layer 2/3 with responding neurons (depth ~120-250 μm). Once the cells were selected, a high resolution (512x512 pixels, 0.74 Hz) image was collected for reference and then fast images (128 × 128 pixels; 11.84 Hz) were collected during longer trials (40 s plus 5-10 s baseline) with 8 s whisker stimulation (0 or 90 Hz). Multiple imaging sessions were conducted on different days for each animal. During some sessions, fast frame scan images were immediately analyzed (see Quantification and Analysis below) to identify rapid astrocyte regions of interest. Line scans were then drawn through these areas and data were collected at ~1500Hz.

In vivo pharmacology

Neuromodulator drugs were dissolved as follows: atropine (Sigma-Aldrich; 0.75mg/mL), trazodone (Sigma-Aldrich; 3mg/mL), and N-(2-chloroethyl)-N-ethyl-2-bromobenzylamine (DSP-4, Tocris; 10mg/mL) were dissolved in 0.9% NaCl. Prazosin (Tocris) was dissolved in dH_2O at 0.5mg/mL and diluted 1:1 with 0.9% NaCl before injection. Metergoline (Sigma-Aldrich; 40mg/mL) was dissolved in DMSO, and each mouse received less than 3uL DMSO/10 g body weight. All drugs were injected I.P. at least 20 min before imaging and all images were acquired within 2 hr of injection. DSP4 was injected I.P. (50 mg/kg) 4-10 days prior to imaging. The same fields of view were imaged for all drugs (but on different imaging days). See Key Resources Table.

SR101 staining

Animals were anesthetized with isoflurane (4% induction, 1.5% maintenance) and sulforhodamine 101 (SR101, 20 mg/kg) was injected intravenously into mice with expression of cyto-GCaMP6s or Lck-GCaMP6f as previously described (Appaix et al., 2012). Images of SR101 and GCaMP were collected up to 100 min after injection, by two-photon microscopy at 900 nm.

Immunohistochemistry

Mice were anesthetized with pentobarbital (>50mg/kg) and transcardially perfused with 2% PFA. Brains were post-fixed in 4% PFA for 3 hr and cryoprotected with 30% sucrose in PBS for 24 hr. Free-floating brain stem sections (40μm) were cut with a freezing microtome and incubated with primary antibodies (rabbit anti-GFAP (Z0334; Dako Cytomation) and chicken anti-GFP (GFP-1020, Aves Labs)) in Tris-Triton (0.2%) + 5% Normal Goat Serum (NGS) overnight at 4°C. Secondary antibodies (goat-anti-rabbit-Cy5 (1:500; Jackson ImmunoResearch) or goat anti-chicken Alexa Fluor 488 (1:500, ThermoFisher) were added and sections were mounted on slides with Fluorescence Mounting Medium (Dako). Images were acquired on a Zeiss Confocal LSM710 microscope.

QUANTIFICATION AND STATISTICAL ANALYSIS

Image analysis was performed using ImageJ and a custom-designed image processing tool box for MATLAB (Cellular and Hemodynamic Image Processing Suite (CHIPS; Barrett et al., 2018; R2014b; MathWorks). For each field of view, all images were spectrally unmixed to reduce potential bleed through of GCaMP or RCaMP1.07, and aligned using a 2D convolution engine to account for motion and x-y drift in time. Background noise was defined as the bottom first percentile pixel value in each frame and was subtracted from every pixel. Regions of interest (ROIs) were selected by 2 methods: our customized implementation of an activity based algorithm (for identification of active astrocyte processes or neuronal dendrites) and manual selection in ImageJ of astrocyte somata/endfeet or neuronal somata ROIs. In the activity based algorithm, a 2D spatial Gaussian filter (σxy = 2 μm) and a temporal moving average filter (width = 0.5 s for cyto-GCaMP6s and 0.1 s for Lck-GCaMP6f/RCaMP1.07) were applied to all images to reduce noise. Active pixels were identified as those that exceeded a moving threshold (mean pixel intensity + 5 SD (for cyto-GCaM6s) or 7 SD (for Lck-GCaMP6f or RCaMP1.07)) and had a peak within a defined time window (0.1689 – 8 s for cyto-GCaMP6s and 0.0845 – 2 s for Lck-GCaMP6f/RCaMP1.07) compared to the preceding 5 s. Active pixels were grouped within space (minimum area of 3.78 μm^2 for cyto-GCaMP6s and 10 μm^2 for Lck-GCaMP6f/RCaMP1.07) and time (1.35 s for cyto-GCaMP6s or 0.169 s for Lck-GCaMP6f/RCaMP1.07). The 3D mask of active pixels was summed along the temporal dimension, normalized, and thresholded (θ = 0.33 for RCaMP1.07 or θ = 0.2 for GCaMP6s/GCaMP6f) to make a 2D activity ROI mask for each channel. Raw image data from pixels within each 2D ROI were statistically compared to pixels surrounding the ROI (p value < 0.05 by one-way ANOVA) to exclude false positives. The signal vector (dF/F) from each ROI was filtered using a moving average filter (3 s averaging for cyto-GCaMP6s, 1.5 s averaging for Lck-GCaMP6, or 2 s averaging for RCaMP1.07) to identify slow, broad peaks (findpeaks function; MATLAB). Short, fast peaks were identified by applying a digital band-pass filter with passband frequencies (f1 = 0.05 Hz and f2 = 0.2 Hz for cyto-GCaMP6s; f1 = 0.05 Hz and f2 = 0.5 Hz for Lck-GCaMP6f; f1 = 0.1 Hz and f2 = 1 Hz for RCaMP1.07) before running the MATLAB findpeaks function. The peak onset latency was calculated from the smoothed signal trace (5 frame moving average) as the first time point when the signal went over the threshold (the mean of the 5 s baseline plus 2.5 times the standard deviation) after the start of stimulation.

During analysis, we defined time windows within our 40 s trial for studying the mean time differences of the neuronal and astrocyte responses to stimulation. These time thresholds were defined by log transforming the distribution (to convert the left

skewed distribution to a normal distribution) of onset latencies and latencies to peak maximum for cyto-GCaMP6s and Lck-GCaMP6f signals. We then determined the upper bound of the 99% confidence interval (2.33*σ) and used this time as our longest time threshold for comparing neuron and astrocyte timings in Figure 1. In Figure 2, we created subsets of astrocyte responses (fast and delayed MDs) based on the median onset time of neurons during stimulation (1.098 s).

We conducted a linear correlation (corrcoef, MATLAB) and cross-correlation (xcorr, MATLAB) analysis to correlate the signal vector (dF/F) from the first 20 s following whisker stimulation for each Lck-GCaMP6f ROI with the vectors from all RCaMP ROIs in the same field of view (corrcoef, MATLAB). We also used the Pythagorean theorem to calculate the distance between the Lck-GCaMP6f/RCaMP1.07 ROI edge indices and selected the minimum value as the distance between the ROI pair. Neuronal ROIs were categorized based on their response amplitudes: high responders were the upper 5^{th} percentile, mid responders were the 50^{th}-95^{th} and low responders were the lower 50^{th} percentile.

All statistics were performed in R (version 3.4.1) using the lme4 package for linear mixed-effects models. As fixed effects, we used stimulus condition (with/without stimulation), ROI type (astrocyte endfoot or process and neuronal somata or dendrites), and astrocyte type (fast or delayed) and also tested the interaction of these effects. As random effects, we had intercepts for individual animals, fields of view, and ROIs. Likelihood ratio tests comparing models with fixed effects against models without fixed effects were used to determine the model with the best fit while accounting for the different degrees of freedom. Visual inspection of residual plots did not reveal any obvious deviations from homoscedasticity or normality. All data were reported and plotted as uncorrected means and standard error of the means. p values for different parameter comparisons were obtained using the multcomp package with Tukey post hoc tests. The ks.test function was used for Kolmogorov-Smirnov test comparisons between distributions and the wilcox.test function was used for Wilcoxon Rank Sum tests of medians.

DATA AND SOFTWARE AVAILABILITY

CHIPS toolbox for MATLAB is freely available on GitHub (https://ein-lab.github.io/) (Barrett et al., 2018).